Characterisation of a smartphone image sensor response to direct solar 305 nm irradiation at high air masses

Igoe, D. P[1,2*]., Amar, A.[1], Parisi, A. V.[1] and Turner, J.[1]

[1] Faculty of Health, Engineering and Sciences, University of Southern Queensland, Toowoomba, Queensland

[2] School of Medicine and Dentistry, James Cook University, Townsville, Queensland

[*] Corresponding author: damien.igoe@usq.edu.au

Abstract

This research reports the first time the sensitivity, properties and response of a smartphone image sensor that has been used to characterize the photobiologically important direct UVB solar irradiances at 305 nm in clear sky conditions at high air masses. Solar images taken from Autumn to Spring were analysed using a custom *Python* script, written to develop and apply an adaptive threshold to mitigate the effects of both noise and hot-pixel aberrations in the images.

The images were taken in an unobstructed area, observing from a solar zenith angle as high as 84° (air mass = 9.6) to local solar maximum (up to a solar zenith angle of 23°) to fully develop the calibration model in temperatures that varied from 2°C to 24°C. The mean ozone thickness throughout all observations was 281 ± 18 DU (to 2 standard deviations). A Langley Plot was used to confirm that there were constant atmospheric conditions throughout the observations.

The quadratic calibration model developed has a strong correlation between the red colour channel from the smartphone with the Microtops measurements of the direct sun 305 nm UV, with a coefficient of determination of 0.998 and very low standard errors. Validation of the model verified the robustness of the method and the model, with an average discrepancy of only 5% between smartphone derived and Microtops observed direct solar irradiances at 305 nm. The results demonstrate the effectiveness of using the smartphone image sensor as a means to measure photobiologically important solar UVB radiation.

The use of ubiquitous portable technologies, such as smartphones and laptop computers to perform data collection and analysis of solar UVB observations is an example of how scientific investigations can be performed by citizen science based individuals and groups, communities and schools.

Keywords: ultraviolet radiation, atmospheric radiation, solar ultraviolet, photobiology, smartphone, CMOS image sensor

Introduction

Research into the damaging influences (Longstreth et al. 1998) and beneficial influences (Piri et al. 2011; Grant, 2008) of solar UV radiation requires the measurement of personal solar UV exposures during normal daily activities. The established measurement techniques range from spectroradiometry, radiometry and dosimetry techniques (Parisi et al. 2004; Cancillo et al. 2005). Recent research has investigated the novel approach of the measurement of narrowband and broadband UV exposures with the CMOS camera sensor in a smartphone (Fung and Wong, 2016; Turner et al., 2016; Igoe and Parisi, 2015; Igoe et al., 2014b).

The use of ubiquitous portable technology, such as smartphones to collect irradiance data and freely available programming tools, such as Python on the equally available laptops and tablets to analyse data provide avenues for participatory Citizen Science involvement in atmospheric UVB observations, with connections to the related public health topics, such as skin cancer mitigation.

Previous research concluded that smartphone image sensors, fitted with narrow passband filters, can detect quantifiable irradiances deep in the UVA waveband (specifically 340 nm to 320 nm) and into the UVB (310 nm) with a modified smartphone image sensor from laboratory monochromatic and solar sources (Wilkes et al. 2016; Igoe and Parisi, 2015). The signal is characterised by very low dark noise signals that is largely unaffected by changes in temperature (Igoe et al. 2014a). Total noise increased with decreasing wavelength and increasing solar zenith angle when observing the direct solar UVA (Igoe and Parisi, 2015). Considering that dark noise in modern smartphone image sensors is negligible (Wilkes et al. 2016; Igoe et al. 2014b; Riutort-Mayol et al. 2012), the likely source is due to temporal noise sources such as pixel photo response and spatial non-uniformity noise across the images (Riutort-Mayol et al. 2012).

Despite significant attenuation of the incident solar UV irradiances due to the outer lens, narrowband signals at 320 nm were found to be quantifiable to be used in smartphone based evaluation of the UVA (Igoe and Parisi, 2015) and quantifiable at 310 nm (Wilkes et al. 2016). The prior research and preliminary observations with a laboratory UV source (Turner et al., 2016) suggest that the attenuated solar irradiances in the UVB waveband ought to be measurable and quantifiable. No previous research has evaluated the direct sun UVB irradiances at 305 nm quantified by a smartphone image sensor. The purpose of this research is to determine the sensitivity, properties and response of a smartphone image sensor in the field to narrowband direct solar UVB irradiation at 305 nm at a range of solar zenith angles, with a focus on high solar zenith angles greater than 60° (air mass = 2).

The wavelength of 305 nm was selected due to the relatively high response at this wavelength for the erythemal action spectrum (CIE, 1998) and the previtamin D_3 action spectrum (CIE, 2006). The 24 hour MED (minimum erythemal dose) measured at 305 nm has been reported as a sensitive indicator of skin type (Kollias et al., 1996). Furthermore, this wavelength is often cited in UVB aerosol studies and is a wavelength used in measurement equipment, such as the Microtops II sunphotometer (Morys et al. 2001) and the ultraviolet multi-filter rotating shadow band radiometer (Wenny et al. 2001) and is a wavelength used in measuring the total ozone column in the Dobson spectrophotometer and other instruments (World Meteorological Organisation, 2012; Wenny et al., 2001). This wavelength is also the focus of measurements of the Quasi-Biennial Oscillation (QBO) in the UVB (Zerefos et al. 2001).

Methodology

Equipment

The smartphone used for direct sun observations at 305 nm was the Sony Xperia Z1 (Sony Corporation, Tokyo, Japan). This phone has a more advanced camera sensor than the one used in the previous research (Igoe and Parisi, 2015). The dark response of all colour channels of the smartphone image sensor at several different ambient temperatures was determined by taking images with the lens completely obscured with black electrical tape (Igoe et al. 2014a). The Xperia Z1 has a 21-megapixel camera using Sony's *Exmor RS* backside-illuminated mosaic image sensor (IMX 230). The image sensor has a diagonal length of 7.487 mm, consisting of square pixels, 1.12 µm across (Sony Corporation, 2015). The image sensor was unmodified and no external sensors were used in the collection of UVB irradiances.

Measurements made by the smartphone were calibrated against a Microtops II sunphotometer (Model E540, Solar Light Inc., USA). The Microtops measures direct sun irradiances at a stated value of 305 nm. The narrowband filter (Solar Light Inc.) used to calibrate the smartphone was the same as that used in the Microtops, and was centred at 305.5 nm with a FWHM (full width at half maximum) of 2 nm. The diameter of the filter was approximately 13 mm and was sufficient to fully cover the smartphone camera lens. For the purposes of this research, this centre wavelength will be referred to as being 305 nm. The outer lens of the smartphone was kept in place and the image sensor responses were made without using any external hardware as has been done with similar studies (Wilkes et al. 2016).

Time and Location

All measurements were performed within one kilometre of the University of Southern Queensland, Toowoomba (elevation 693 m; latitude 27°36'S longitude 151°55'E), Queensland, Australia. A set of five measurements were taken every 20 minutes between local dawn and solar maximum, from April to October 2016. Data was collected over 2 days for the calibration of the smartphone camera and over 5 days for the validation. The solar zenith angles (θ_{SZA}) over the measurement period were 84° to 23°.

Field measurements

The measurement focus was on angles corresponding to high solar zenith angles (θ_{SZA}), extending beyond an air mass of 2 ($\theta_{SZA} > 60°$), thus exceeding the limit demonstrated by earlier research (Igoe and Parisi, 2015). Images were taken from the earliest time that Microtops readings could be taken to ensure the visibility of the solar image on the smartphone image sensor. All observations were performed on days when the sun was not obscured by clouds.

The Microtops was used to measure the direct solar irradiance at 305 nm, the ozone layer thickness in Dobson Units (DU) and the aerosol optical thickness (AOT) at 340 nm. The latter was included as a proxy to the aerosol conditions, as a direct measurement at 305 nm was not available with the current device. A Langley Plot is used to confirm constant conditions with the overall atmospheric optical depth and image sensor sensitivity across the observations (Parisi et al. 2004).

The Microtops was securely mounted on a sturdy camera tripod (Figure 1) in a yard that had no obstructions to prevent any direct observation of the sun for all measurements.

Figure 1: The Microtops II Sunphotometer securely mounted on a camera tripod in an area with an unobstructed view of the direct sun at various zenith angles.

The 305 nm filter was secured over the camera lens of the Sony Xperia Z1, using Blutak to hold the filter in place (Figure 2 left), then having black felt surround the filter to prevent light leakage from contaminating the images. The felt and filter were further secured using black electrical tape to eliminate light leakage (Figure 2 right).

Figure 2: Emplacement of the 305 nm filter on the Sony Xperia Z1, secured using Blutak (left), then surrounded by black felt to prevent light leakage and held firm using black electrical tape (right).

The direct sun images were taken by aligning the smartphone with the Microtops for each observation. Care was taken to ensure that the Microtops input optics and the camera sensor and filter on the smartphone were in direct alignment (Figure 3) with the direct sun. Smartphone measurements entail taking data from the area covered by the image of the solar disk. These pixels are mostly the result of direct solar irradiance, but do have the influence of a small amount of diffuse. As it is impractical to separate the amounts using a smartphone, for simplicity these measurements are referred to as ‘direct solar irradiance’. For experimental simplicity, each photo was saved in the default JPEG format for smartphones, with all settings set to automatic. Measurements from the Microtops were taken at the same time.

Figure 3: Alignment of the smartphone filtered camera to the same direction as the input optics of the Microtops II sunphotometer. Confirmation of the correct targeting can be seen with the white dot in the centre of the Sun target on the sunphotometer.

The smartphone images were downloaded to a computer and were initially analysed using the freely accessible *ImageJ* software (imagej.nih.gov) to visually ascertain the distribution of pixel values of each colour channel and to observe a cross sectional profile of pixel values through the solar image. This step helps select which of the colour channels will be focused on. Due to the precision in aligning the smartphone with the Microtops, the solar disk was at the same position in each photo.

Langley Plot

To ensure consistency in atmospheric optical conditions despite variations in ozone and aerosol optical depths, a Langley Plot was derived from all calibration and validation 305 nm irradiance data collected from the Microtops plotted against the air mass of when they were measured. The Langley Plot was determined by the Beer-Lambert Law (Bigelow et al., 1998):

$$\ln I_{305} = \ln I_{0,305} - m\tau \qquad [1]$$

where $\ln I_{305}$ is the natural log of the solar irradiance measured from the Microtops at 305 nm; $\ln I_{0,305}$ is the natural log of the extraterrestrial irradiance (air mass = 0); m is the air mass and τ is the optical depth, which is the gradient when $\ln I_{305}$ is plotted against m (Bigelow et al. 1998).

Image analysis

Pixel values (or 'digital numbers') cannot be negative values and their distributions tend to be log-normal (Igoe et al. 2014a). This necessitates the use of geometric mean and standard deviations in all analyses (Limpert et al. 2001). These statistics form the basis of an adaptive threshold developed using the *Python* programming language for use in image analysis. This adaptive threshold was employed to statistically analyse pixel data of the imaged solar disk that had pixel values that were well above the background noise levels.

Analysis and retrieval of important statistical information was performed using a custom written *Python* script (developed by D. Igoe). The script performed the analysis with the following steps:

1. The user is prompted to open an image file, where on clicking the button, the open-file dialog box is opened and the image can be manually selected from where it has been saved.
2. The script then selects the most visible colour channel array (confirmed from earlier *ImageJ* based observations).
3. A 5 x 5 median filter is applied to remove the presence of hot pixels. A hot pixel represents a pixel with a value far above the mean pixel value (Pain et al. 2005). This is an important consideration for any imaging device with very small pixel sizes (Chapman et al. 2016).
4. Necessary image statistics are calculated, the geometric mean (μ^*), used as a baseline; the geometric standard deviation (s^*) and the maximum pixel value (*max*).
5. The adaptive threshold is determined to allow selection of the pixels corresponding to the image of the sun. For simplicity, the adaptive threshold is calculated as being the upper bound of the 4th standard deviation from the mean, for geometric statistics, this is calculated using equation 2 (Limpert et al. 2001):

$$threshold = \mu^* \times (s^*)^4 \quad [2]$$

The 4th standard deviation was selected based on initial observations that the solar disk occupied less than 0.003% of the total image, corresponding to the amount of the pixels expected to be distributed above the upper bound of the threshold.

6. An algorithmic ‘mask’ is applied, which excludes all pixel values below the calculated adaptive threshold from any further analysis, so only pixel values above the threshold are considered.
    - A data validation step is included, declaring any image where *max* < *threshold* as invalid, as these are considered for this research to be comparatively underexposed images. This data validation is crucial to prevent the script from crashing.
7. The mean and standard deviation of the pixel values retained above the mask for each image are recorded and provided for calibration in *Excel*.

The development of the simple Python algorithm allowed quick and efficient data collection to be used for final calibration modelling in Excel. This calibration modelling is a crucial step if different smartphone model is used, as previous similar research found that each device responds differently to solar UV irradiation (Igoe et al. 2014b).

Smartphone calibration

When viewing the sun ‘off axis’ from zenith, with an air mass greater than 1, the irradiances are analogous to the trigonometric transformations that occur with field darkening, reducing it by a factor of $\cos^4 \theta_{SZA}$ (Hauftecker, 2000). The $\cos^4 \theta_{SZA}$ reduction at increased air masses was applied to the average grayscale, red, green and blue pixel values (*Y*, *R*, *G* and *B* respectively) for each smartphone image (Igoe et al. 2014b). Multiplying by this value provides a corrected image sensor response value for each image, reduced in response to increased air mass (Igoe et al. 2013). A further correction to account for the variations in the Earth-Sun distance (D^2), based on the observation day of the year (*doy*) is multiplied to the corrected image sensor pixel values, as shown in equation 3 (Porter et al. 2001).

$$D^2 = \{1 - 0.01673\cos[0.017201(doy - 4)]\}^2 \qquad [3]$$

The natural log of direct solar irradiances at 305 nm measured using the Microtops II sunphotometer ($\ln I_{305}$) was used to calibrate the corresponding corrected average of the image sensor pixel values for each image. The resulting proportionality relationship, based on earlier research (Igoe et al. 2014b) and adapted as represented in equation 4 was applied.

$$\ln I_{305} \propto f[\ln(\{Y, R, G, B\}D^2\cos^4\theta_{SZA})] \qquad [4]$$

where $\ln I_{305}$ is the natural log of the solar irradiance at 305 nm measured by the Microtops and $\ln(\{Y, R, G, B\}D^2\cos^4\theta_{SZA})$ represents the smartphone derived colour pixel values for the respective red (*R*), green (*G*) and blue (*B*) image sensor responses and grayscale (*Y*), calibrated with a function *f*.

<u>Validation</u>

The validity of the model derived in the calibration stage (equation 4) was tested by applying the corrected colour channel and grayscale pixel values derived calibration equations to determine the magnitude of the corresponding irradiances at 305 nm for a set of data collected to validate the model. These values were confirmed by plotting a linear goodness-of-fit relationship with the corresponding Microtops measurements (Riutort-Mayol et al. 2012).

Noise analysis

Dark noise (response) was calculated using the average pixel values for each of the 3 colour channels (red, green and blue) and their respective standard deviations were determined by using a custom *Python* script that also evaluated the prevalence of 'hot-pixel' values. The number of hot-pixels were consistent for all photos at a frequency of approximately 0.002% of the total pixels in each image. There was no pattern discernible in the spatial distribution of the hot pixels.

Additionally, the average signal to noise ratio (SNR) was performed on all 3 colour channels and grayscale values for comparison to discern if there is a 'trade-off' in terms of SNR with sensitivity to lower wavelengths (Wilkes et al. 2016). The SNR was calculated using the '20log' rule (Nakamura, 2006).

$$SNR = 20\log\left(\frac{\mu}{\sigma}\right) \quad [5]$$

where μ is the mean pixel value and σ is the corresponding 2nd standard deviation. Positive values represent a higher signal as opposed to negative values, which represent noise.

The standard deviation is described as an indicator of sensor noise (Riutort-Mayol et al. 2012). As several different sets of measurements were taken over different days in different seasons, the standard deviation of the mean, or standard error (Zalewski, 1995), is calculated as the noise indicator, based on the 2nd standard deviation or approximately the 95% confidence interval – for simplicity, this will be referred to as 'standard error' for the remainder of the paper.

Therefore, a measure of the total noise will be performed across pixel values above the threshold for each image to a 95% confidence level; this will be compared to the subsequent irradiances to characterise the sensor noise (Riutort-Mayol et al. 2012). The standard error derived from smartphone observations will be compared to the $ln(I_{305})$ derived from the Microtops, in an interaction plot (Riutort-Mayol et al. 2012). A test to determine if the increase in solar irradiance (measured by $ln(I_{305})$) results in an increase in sensor noise, approximated as the standard error (Riutort-Mayol et al. 2012; Kutner et al. 2004). The test will also determine if the increase in solar irradiance results in heteroscedasticity, or increased variability, on the sensor noise.

Results and Discussion

All Microtops observations taken at 305 nm using the Microtops (from the calibration and validation stages) are plotted against their corresponding air masses in the Langley Plot (Figure 4).

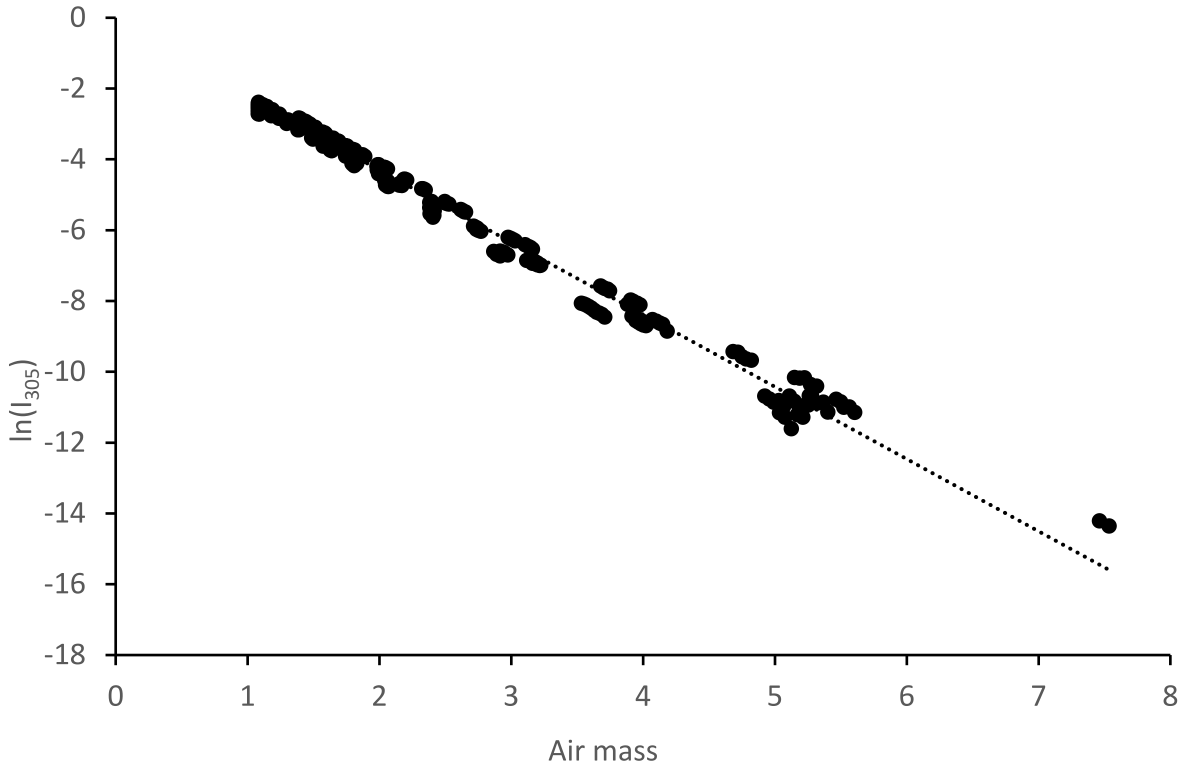

Figure 4: Langley Plot for all the Microtops irradiances compared to their corresponding air masses collected during the research (n = 449).

The very high correlation (R^2 = 0.99) confirms that a 'constant sky' prevailed throughout the calibration and validation observations, despite variations in the range of ozone optical depth (263-337 DU). Despite there being considerable variation in the range of observed aerosol optical thicknesses at 340 nm (0.12-0.38), this does not appear to greatly influence the observations made at 305 nm.

All 3 colour channels and grayscale pixel value or digital number data distributions were plotted to ascertain if their distributions were at least approximately normally distributed (Gaussian), as shown in figure 5 for an image for an SZA of 53°.

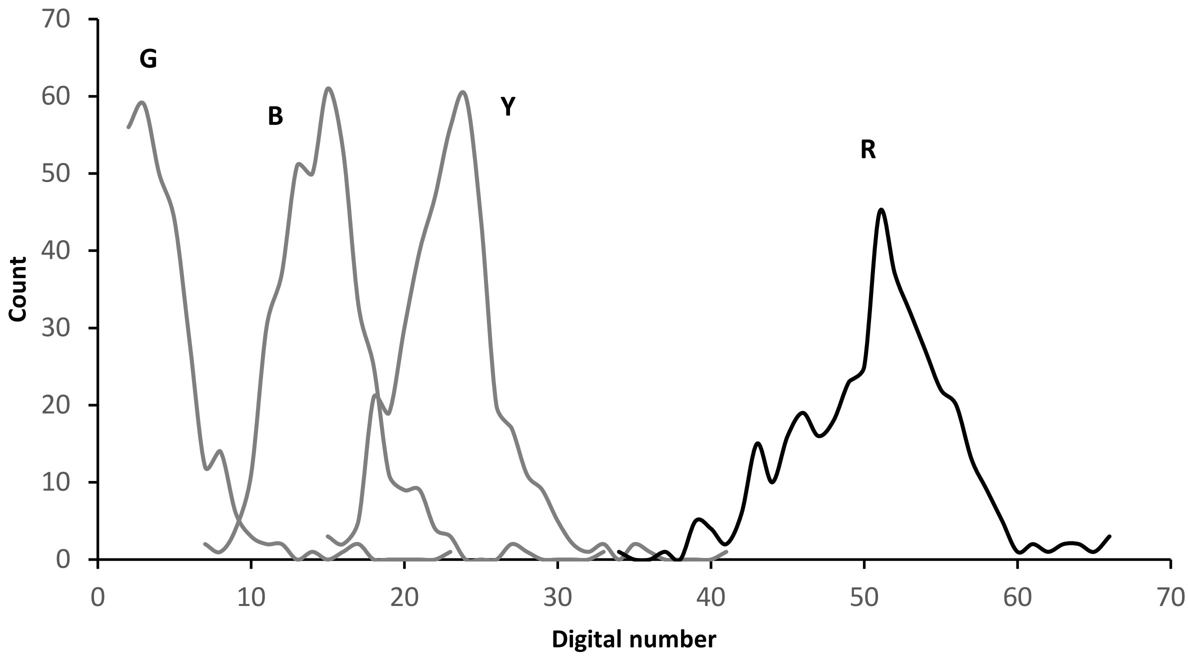

Figure 5: Sample distribution for red (R), green (G), blue (B) and grayscale (Y) pixel values or digital numbers for an image with an SZA of 53°.

The sample distribution shows that the blue channel and grayscale pixel values have a clear approximation to a normal distribution, red slightly less so and the green channel is truncated, indicating that much of that channel's distribution is indistinguishable from the fixed pattern noise. These patterns were largely repeated for all measurements with little variation. As all colour channels pixel values have a distribution that can be approximated to normal, the mean, standard deviations and standard errors can be determined (Yoo et al. 2007; Zalewski, 1995).

In calculating the dark response (noise), the average mean and 2 standard deviations (representing approximately 95.5% of pixel values) for each colour channel pixel values were consistent across all observations and conditions (temperature range of 2°C to 24°C), consistent with the previously reported temperature invariance of dark noise (Igoe et al. 2014a). Table 1 summarises the statistics for each colour channel noise level.

Table 1: Comparison of mean dark noise pixel values for each colour channel and respective standard deviations (n = 123).

	Colour channel		
	Red	**Green**	**Blue**
Mean pixel value	2.94	0.16	1.41
2 standard deviations	1.84	0.93	1.53

Although the standard deviation is greater than the mean for the green and blue channels, the pixel values will never be in the impossible state of being negative owing to the geometric nature of lognormal distributions (Limpert et al. 2001). The upper pixel dark noise values for the red, green and blue colour channels are approximately 9.92, 0.19 and 3.31 respectively.

There is a very clear difference between the signal to noise ratio (SNR) of the green colour channel pixel values as compared to the red and blue channels. The SNR calculation demonstrates that the green channel is mostly indistinguishable from noise, resulting in the grayscale value being a false positive signal, as grayscale is calculated from mostly the green channel (Alala et al. 2014). The SNR distributions for the red, green and blue colour channels pixel values for 449 images are shown in Table 2.

Table 2: Signal to Noise ratio (SNR), by the 20log rule, for all colour channels pixel values, n = 449.

	Colour channel		
	Red	**Green**	**Blue**
Mean SNR	16.3	-0.6	12.1
Standard deviation (95% confidence level)	3.6	5.2	3.5

To be able to develop a model that would include the low-light conditions that occur at high air masses (> 2), a colour channel with a signal distinguishable from background noise is required. Figures 6a and 6b display the pixel values of a cross section of the pixels through an image of the sun and surrounding areas taken at dawn and midday respectively.

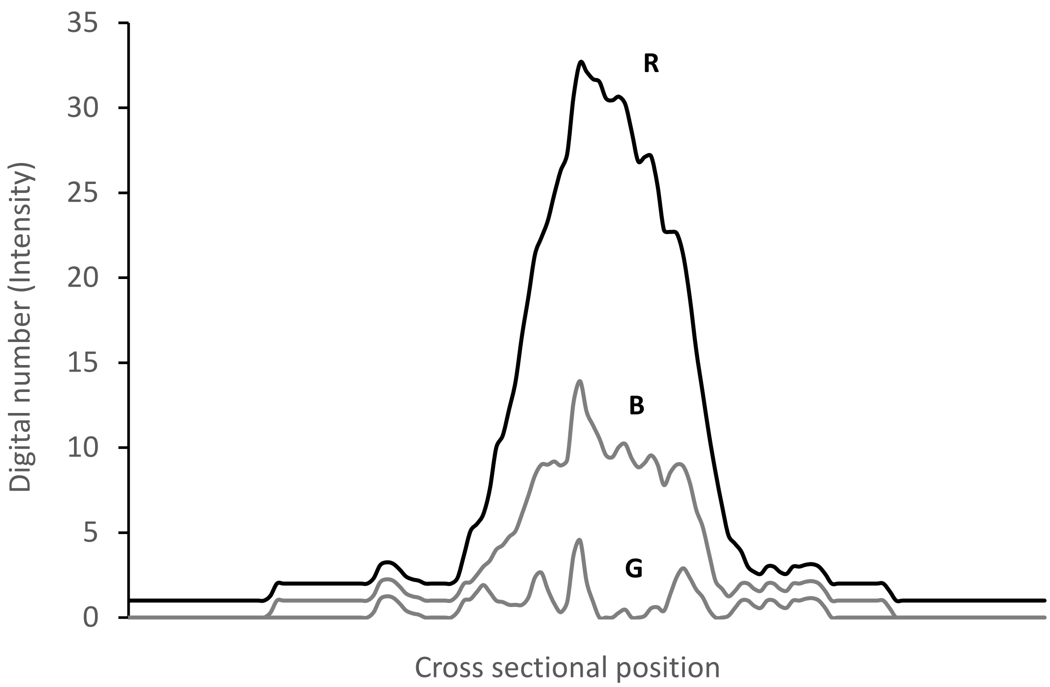

Figure 6a: The pixel values of a cross section of the pixels through the sun image and surrounding areas taken at dawn (red = R, green = G and blue = B) for an SZA of 81°.

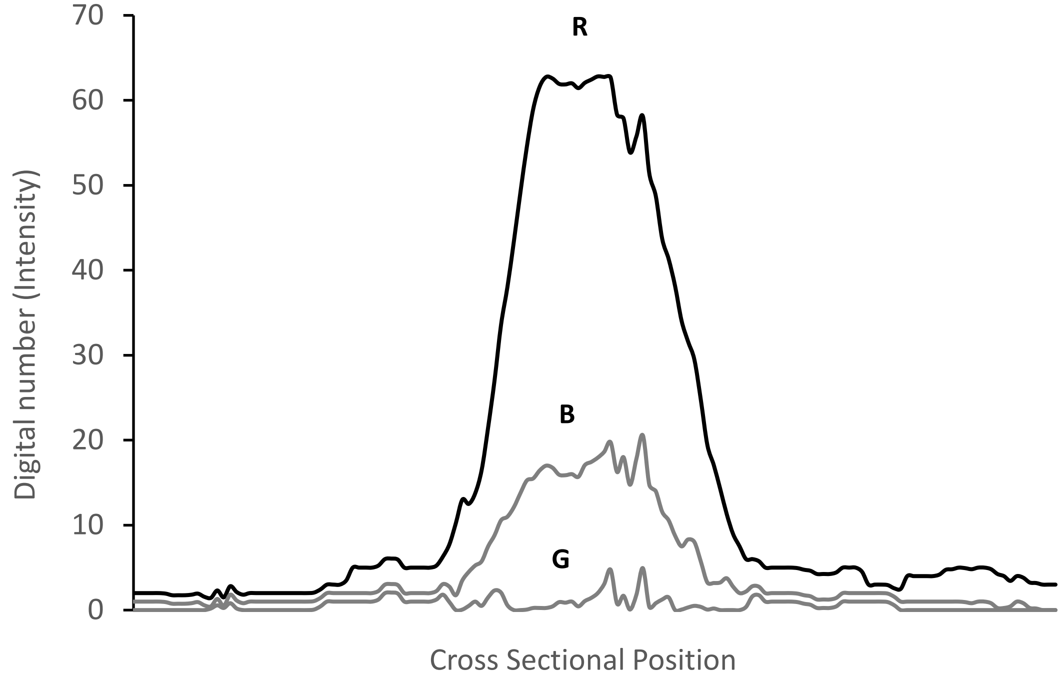

Figure 6b: The pixel values of a cross section of the pixels through the sun image and surrounding areas taken at midday (red = R, green = G and blue = B) for an SZA of 27°.

The cross sections in Figures 6a and 6b clearly demonstrate that the red channel for the smartphone used provides the clearest signal with the greatest count of measurable pixels at both dawn and midday. The blue channel possesses considerably lower pixel values at both times and has a measurably smaller cross-sectional diameter. The green channel is further shown to be indistinguishable from the background noise. Therefore, only the red channel will be considered for further analysis.

<u>Smartphone Calibration</u>

All solar images were analysed using the *Python* script and the adaptive threshold applied. The mean red pixel value above the threshold for each image and the corresponding standard deviation (to 95% confidence level) were calibrated against corresponding Microtops irradiance observations using *Microsoft Excel*.

Two models were considered, linear and quadratic. The coefficient of determination (R^2) was determined for each as a gauge for the model's precision, the linear model had R^2 = 0.971, compared to the quadratic model with R^2= 0.998; therefore, the quadratic model will be considered for further analysis. Figure 7 shows the quadratic calibration model comparing the smartphone derived $ln(I_{305})$ values for the red channel calibrated against the consequent values obtained from Microtops' observations.

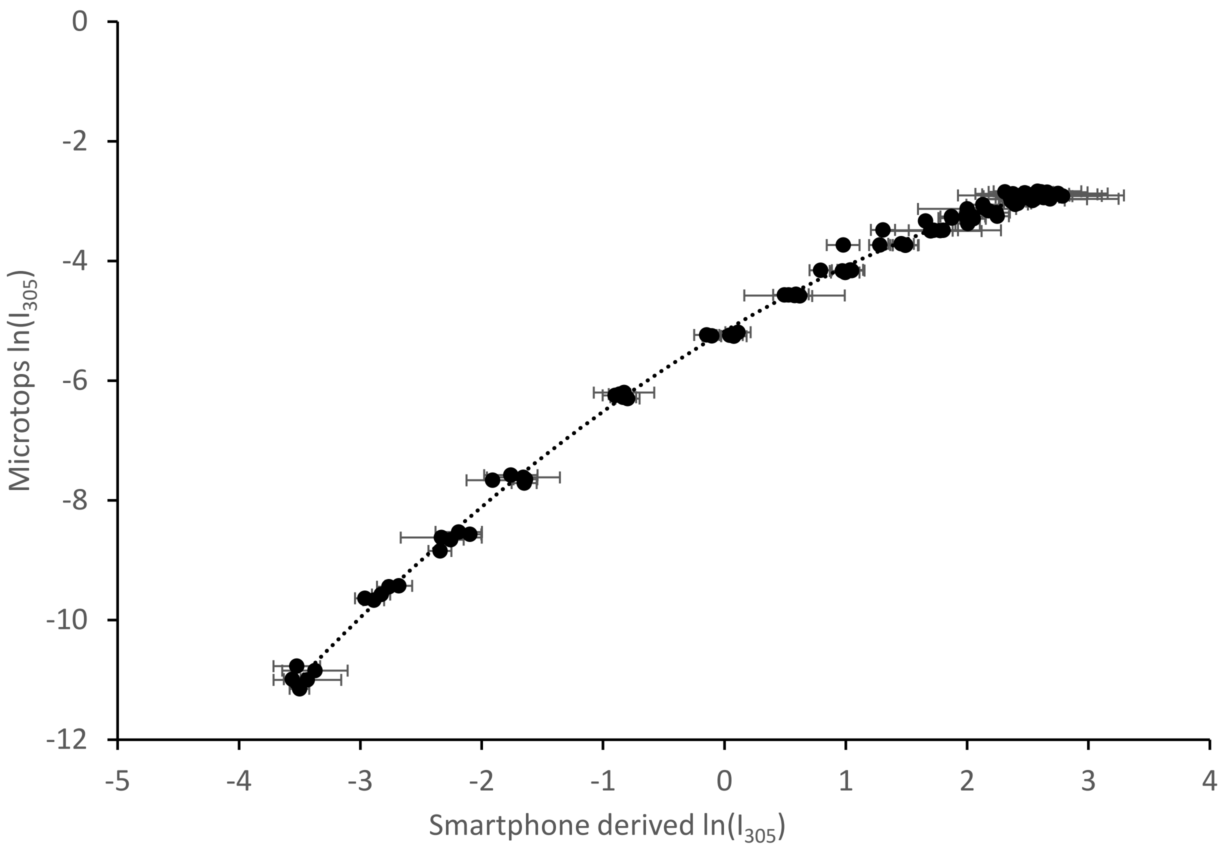

Figure 7: ln(I_{305}) values derived from smartphone observations compared to those observed with the Microtops (n = 94). The error bars indicate the standard error.

The red (R) colour channel pixel values calibrated model is:

$$\ln I_{305} = -0.1274x_R^2 + 1.2126x_R - 5.1764 \qquad [6]$$

where x_R represents $\ln(\{R\}D^2 \cos^4 \theta_{SZA})$ from equation 4 and the subscript R indicates the average red colour channel pixel value/digital number for each image.

Validation

Further observations were made to validate the model in equation 6. Figure 8 compares the Microtops measured values of $\ln I_{305}$ to those derived using the quadratic model from the calibration of the smartphone. The error bars represent the standard error. The solid line is the 1:1 relationship.

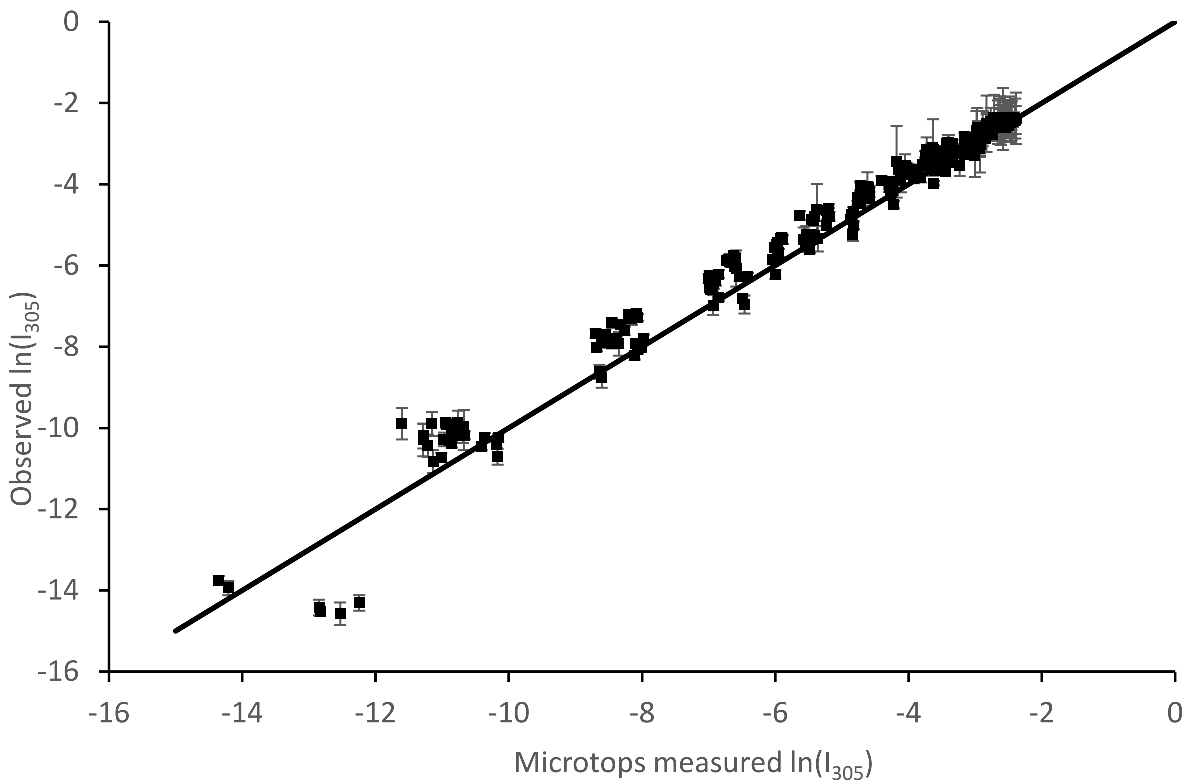

Figure 8: Comparison of smartphone derived values (y axis) for $\ln I_{305}$ to the Microtops measured values for the red channel quadratic model (n = 355).

Figure 8 demonstrates a close agreement between the values derived from the Microtops and those from the smartphone, with correlations of 0.98. Average discrepancies for data derived from the smartphone for the red channel were below +5% from those derived from the Microtops in a range consistent with conventional equipment (Cancillo et al. 2005; Zerefos et al. 2001). The trends indicate an increase in standard error with an increase in irradiance and an increase in scattering as irradiance increases.

The standard error calculated for the illuminated images were mostly below 1, increasing from an average of approximately 0.2 at lower irradiances. The trend in standard error can be seen in Figure 9. The increase in standard error indicates that the image sensor has become more susceptible to photon-induced noise at higher irradiances (Riutort-Mayol et al. 2012), a trend that is consistent with the error bars in the validation chart (Figure 8).

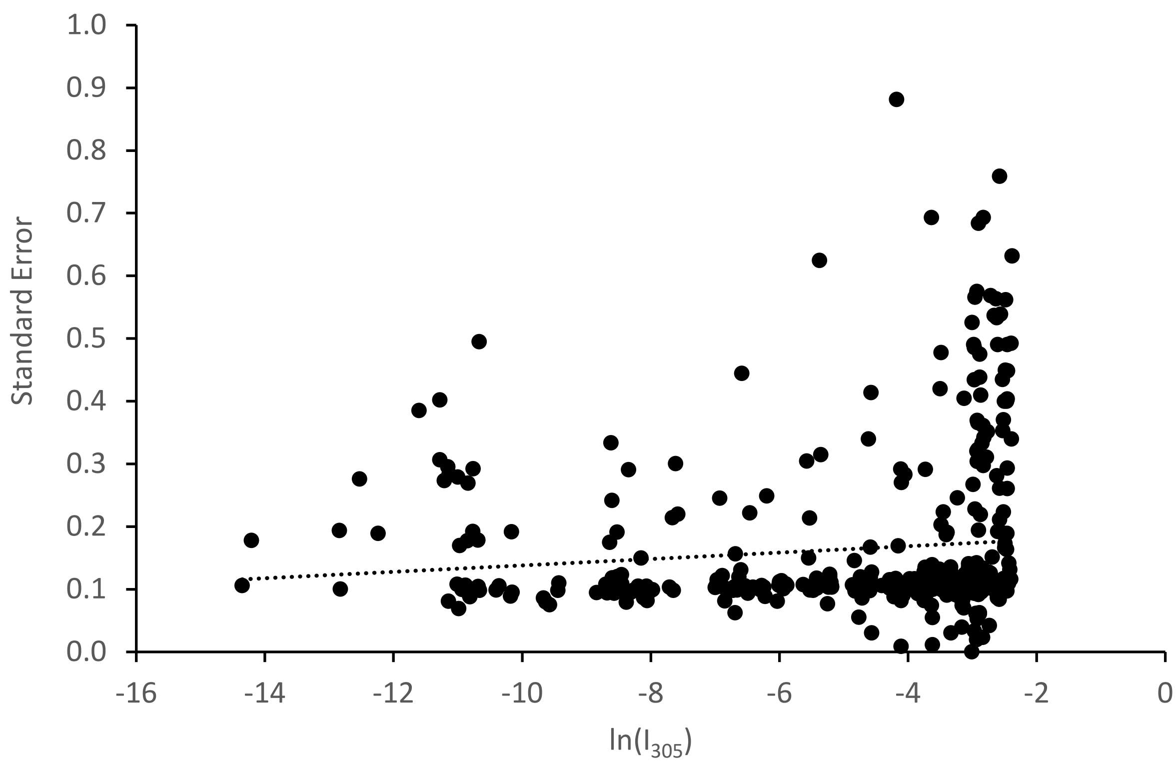

Figure 9: Interaction plot of smartphone derived standard error vs. $\ln(I_{305})$ indicating a greater susceptibility to photon-induced noise as $\ln(I_{305})$ increases.

The data displayed in the interaction plot (Figure 9) shows a heteroscedastic relationship between the noise induced on the smartphone image sensor (approximated by the standard error values) and increasing irradiance as the sun approached local solar maximum (approximated by *$\ln(I_{305})$*

values). This trend indicates that as the air mass decreased, the irradiance increased causing a noticeable increase in photon-induced pixel noise on the image sensor.

Conclusion

This research, for the first time, quantifies the smartphone image sensor response to direct solar clear sky irradiances at 305 nm to an air mass of 9.6, showing that an inexpensive portable smartphone camera sensor can be employed to detect short wavelength 305 nm direct UV at low irradiances. This was achieved by analyzing each colour channel's response, determining that the red channel yielded the least amount of noise and the greatest quantifiable signal. Validation observations of the quadratic calibration model demonstrated the robustness of the model with an average discrepancy below 5% between smartphone derived direct sun irradiances and Microtops based measurements. The use of a relatively low cost and widely accessible smartphone camera sensor for direct sun UV irradiances measurements at 305 nm has the potential for use in UV measurements in photobiology and associated skin cancer public health research. Further research and development would be to develop an app to automate the data collection and analysis process.

Acknowledgements

We would like to acknowledge the Faculty of Health, Engineering and Sciences of the University of Southern Queensland for the purchase of the smartphone used in this paper.

References

Alala, B. Mwangi, W. and Okeyo, G. 2014, Image Representation using RGB Color Space, *International Journal of Innovative Research and Development*, vol. 3, issue 8, pp. 322-328

Bigelow, D. Slusser, J. Beaubien, A. and Gibson, J. 1998, The USDA Ultraviolet Radiation Monitoring Program, *Bulletin of the American Meteorological Society*, vol. 79, issue 4, pp. 601-615

Cancillo, M. Serrano, A. Anton, M. Garcia, J. Vilaplena, J. and de la Morena, B. 2005, An Improved Outdoor Calibration Procedure for Broadband Ultraviolet Radiometers, *Photochemistry and Photobiology*, vol. 81, pp. 860-865

Chapman, G. Thomas, R. Coelho, K. Meneses, S. Yang, T. Koren, I. and Koren, Z. 2016, Increases in Hot Pixel Development Rates for Small Digital Pixel Sizes, *Electronic Imaging, Image Sensors and Imaging Systems*, vol. 6, pp. 1-6

CIE (International Commission of Illumination), 1998, *Erythema Reference Action Spectrum and Standard Erythema Dose*, Vienna: CIE Central Bureau

CIE (International Commission o Illumination), 2006, *Action Spectrum for the Production of Previtamin D3 in Human Skin*, Vienna:CIE Central Bureau

Fung, C. and Wong, M. 2016, Improved Mobile Application for Measuring Aerosol Optical Thickness in the Ultraviolet A Wavelength, *IEEE Sensors Journal*, vol. 16, no. 7, pp. 2055-2059

Grant, W. 2008, The Effect of Solar UVB Doses and Vitamin D Production, Skin Cancer Action Spectra, and Smoking in Explaining Links between Skin Cancers and Solid Tumours, *European Journal of Cancer*, vol. 44, pp. 12-15

Hauftecker, H. 2000, Radiometry of Imaging. In Jahne and Hauftecker (eds), *Computer Vision and Applications*, San Diego, Academic Press Inc.

Igoe, D. and Parisi, A. 2015, Broadband Direct UVA Irradiance Measurement for Clear Skies Evaluated using a Smartphone, *Radiation Protection Dosimetry*, vol. 167, issue 4, pp. 485-489

Igoe, D. Parisi, A. and Carter, B. 2014a, A Method for Determining the Dark Response for Scientific Imaging with Smartphones, *Instrumentation Science and Technology*, vol. 42, issue 5, pp. 586-592

Igoe, D. Parisi, A. and Carter, B. 2014b, Smartphone-based Android App for Determining UVA Aerosol Optical Depth and Solar Irradiances, *Photochemistry and Photobiology*, vol. 90, issue 1, pp. 233-237

Igoe, D. Parisi, A. and Carter, B. 2013, Evaluating UVA Aerosol Optical Depth using a Smartphone Camera, *Photochemistry and Photobiology*, vol. 89, issue 5, pp. 1244-1248

Kollias, N. Malallah, Y. al-Ajmi, H. Bager, A. Johnson, B. and Gonzalez, S. 1996, Erythema and Melanogenesis Action Spectra in Heavily Pigmented Individuals as Compared to Fair-skinned Caucasians. *Photodermatology, Photoimmunology, Photomedicine*, vol. 12, issue 5, pp. 183-188

Kutner, M. Nachtsheim, C. Neter, J. and Li, W. 2004, *Applied Linear Statistical Models*, 1st Ed. New York, McGraw-Hill

Limpert, E. Stahel, W. and Abbt, M. 2001, Log-normal Distributions Across the Sciences: Keys and Clues, *BioScience*, vol. 51, issue 5, pp. 341-352

Longstreth, J. de Gruijl, F. Kripke, M. Abseck, S. Arnold, F. Slaper, H. Velders, G. Takizawa, Y. and van der Luen, J. 1998, Health Risks, *Journal of Photochemistry and Photobiology B: Biology*, vol. 46, issue 1-3, pp. 20-39

Morys, M. Mims III, F. Hagerup, S. Anderson, S. Baker, A. Kia, J. and Walkup, T. 2001, Design, Calibration and Performance of MICROTOPS II Hand-held Ozone Monitor and Sun Photometer, *Journal of Geophysical Research*, vol. 106, issue D13, pp. 14573-14582

Nakamura, J. 2006, Basics of Image Sensors. In J. Nakamura (ed) *Image Sensors and Signal Processing for Digital Still Cameras*, CRC Taylor and Francis

Pain, B. Cunningham T. Hancock, B. Wrigley, C. and Sun, C. 2006, Excess Noise and Dark Current Mechanisms in CMOS Imagers. In *IEEE Workshop on CCD's and Advanced Image Sensors*, Karuizawa, Japan, June 2006

Parisi, A. Sabburg, J. and Kimlin, M. 2004, *Scattered and Filtered Solar UV Measurements*, Dordrecht, Kluwer Academic Publishers.

Piri, E. Babaeian, M. Tavassoli, A. and Esmaeilian, Y. 2011, Effects of UV Irradiation on Plants, *African Journal of Microbiology Research*, vol. 5, issue 14, pp. 1710-1716

Porter, J. Miller, M. Pietras, C. and Motell, C. 2001, Ship-based Sun Photometer Measurements using Microtops Sun Photometer, *Journal of Atmospheric and Oceanic Technology*, vol. 18, pp. 765-774

Riutort-Mayol, G. Marques-Mateu, A. Segui, A. and Lerma, J. 2012, Grey Level and Noise Evaluation of a Foveon X3 Image Sensor: A Statistical and Experimental Approach, *Sensors*, vol. 12, pp. 10339-10368

Sony Corporation, 2015, *Sony Product Brief: IMX 230 Overview*, http://www.sony-semicon.co.jp/products_en/IS/sensor1/img/products/ProductBrief_IMX230_20150427.pdf Accessed 3rd November, 2016

Tedeschi, L. 2006, Assessment of the Adequacy of Mathematical Models, *Agricultural Systems*, vol. 80, issue 2-3, pp. 225-247

Turner, J. Parisi, A. Igoe, D. and Amar, A. 2016, Detection of UVB Radiation using an Existing Internal Smartphone Sensor, *submitted*

Wenny, B. Saxena, V. and Frederick, J. 2001, Aerosol Optical Depth Measurements and their Impact on Surface Levels of Ultraviolet-B Radiation, *Journal of Geophysical Research*, vol. 106, issue D15, pp. 17311-17319

Wilkes, T. McGonigle, A. Penny, T. Taggart, A. White, B. Bryant, R. and Willmott, J. 2016, Ultraviolet Imaging with Low Cost Smartphone Sensors: Development and Application of a Raspberry Pi Based UV Camera, *Sensors*, vol. 16, issue 10

WMO (World Meteorological Organisation), 2012, *Guide to Meteorological Instruments and Methods of Observation*, No. 8 CIMO Guide, Geneva: World Meteorological Organisation

Yoo, Y. Lee, S. Choe, W. and Kim, C. 2007, CMOS Image Sensor Noise Reduction Method for Image Signal Processor in Digital Cameras and Camera Phones. In R. A. Martin, J. M. DiCarlo and N. Sampat (eds) *Digital Photography III*, SPIE

Zalewski, E. 1995, Radiometry and Photometry. In M. Bass, E. van Stryland, D. Williams and W. Wolfe (eds) *IVPV Handbook of Optics*, McGraw-Hill

Zerefos, C. Balis, D. Tzortziou, M. Bais, A. Tourpali, K. Meleti, C. Bernhard, G. and Herman, J. 2001, A Note on the Interannual Variations of UV-B Erythemal Doses and Solar Irradiances from Ground-based and Satellite Observations, *Annales Geophysicae*, vol. 19, pp. 115-120